Quantitative Analysis of Multi-Scale Heterogeneities in Complex Electrode Microstructures

Rubayyat Mahbub,[1,2,§] William K. Epting,[1,3] Tim Hsu,[1,2] Jerry H. Mason,[1,3] Minzheng Feng,[2] Noel T. Nuhfer,[2] Harry W. Abernathy,[3,4] Gregory A Hackett,[4] Shawn Litster,[1,2,5] Anthony D. Rollett,[1,2] and Paul A. Salvador[1,2,*]

[1] U.S. DOE National Energy Technology Laboratory, Pittsburgh, PA 15236, USA

[2] Department of Material Science and Engineering, Carnegie Mellon University Pittsburgh, Pennsylvania, 15213, USA

[3] Leidos Research Support Team, Morgantown, WV 26507, USA

[4] U.S. DOE National Energy Technology Laboratory, Morgantown, WV 26505, USA

[5] Department of Mechanical Engineering, Carnegie Mellon University Pittsburgh, Pennsylvania, 15213, USA

* Corresponding Author: paul7@andrew.cmu.edu, 412-268-2702

Abstract

A semi-empirical model is developed to quantitatively characterize electrode heterogeneities over the micro- and mesoscales, specifically between the relationship of the mean-squared normalized variance in the volume fraction, $(\frac{\sigma_{\Phi_V}}{\bar{\Phi}_V})^2$, and the mean particle size normalized linear dimension, $\frac{L}{\bar{a}_N}$. The model was developed analyzing data from five large-volume physical reconstructions – collected using Xe-plasma focused ion beam with SEM (PFIB-SEM) – of several commercial cell electrodes and from unique sets of synthetic microstructures designed to have controlled distributions in particle size and local volume fractions. When comparing physical reconstructions from distinct regions of the same electrode, millimeter length scale heterogeneities are also observed, even in microstructures with limited mesoscale variability. While the model is developed using synthetic microstructures, it is used to quantify three different types of heterogeneities in the commercial cells. The potential origins are discussed with respect to variations in particle size distributions in feedstocks and to phase distributions related to fabrication processes; the potential performance impacts are discussed with respect to an effective medium theory model. The characterization and analytical methodologies and model presented can support the design and development of improved electrodes.

Keywords: Fuel Cell Materials, Microstructures, Heterogeneity, SOFC, Quantitative Model

1. Introduction

Electrode microstructures in electrochemical energy conversion devices have always been of interest to scientists working towards cell performance maximization,[1–10] because microstructure and performance are closely linked. This applies to solid oxide fuel cells (SOFCs), which possess the advantages of generating electricity with great efficiency and with high fuel flexibility, as well as the capability to recycle high temperature waste heat produced during operation.[3–5,7,8,11] Commercialization of SOFCs is still limited due to several factors, including their insufficient reliability and low durability, performance parameters associated directly with the complex electrode microstructures of SOFCs.[6–10,12] Thus, the path to commercialization can be shortened by better determination of the inter-relationship between the electrode fabrication and its resulting structure and properties.

Electrode microstructures in SOFCs must efficiently carry out species transport and electrochemical reactions. Many are three-phase composites of an electron-conducting phase (ECP), an ion-conducting phase (ICP), and gas permeable pores (GPP).[3–10,12] In high-performance electrodes, all the three phases are interconnected in three dimensions (3D), with characteristic feature diameters, a, on the scale of hundreds of nanometers, resulting in fast transport of ions, electrons, and gas to/from a high density of reaction sites, or triple phase boundaries (TPBs).[13,14,23,15–22] Clearly, the three dimensional (3D) distribution of local microstructural features dictates the transport and reaction rates, and in turn the local current densities and electrochemical potentials, thereby influencing electrochemical performance and degradation related phenomena.[20,24–28] Over the past ten years, methods to quantify the 3D microstructure have been developed, primarily using serial sectioning with a Ga focused ion beam (Ga FIB) combined with scanning electron microscopy (SEM)[10,12,35–39,13,15,29–34] or using nanoscale x-ray computed tomography (nano-CT).[27,37,46–49,38–45] The majority of these works considered reconstructed volumes having linear dimensions on the order of 10 – 30 μm, which is an assumed appropriate volume to characterize the microscale variations in cells built from uniformly distributed nanoscale powders having narrow particle size distributions. However, there is no evidence that commercial cells (or most SOFCs, for that matter) conform to such an ideal. We previously reported on 3D microstructures in commercial fuel cell electrodes, using both Ga FIB-SEM[50] and computed tomography[47] methods, that did not conform to this ideal, but could not capture large enough volumes to fully quantify distributions over longer length scales.

More recently,[51–53] we demonstrated that serial sectioning with a Xe plasma (P) FIB-SEM could be used to reconstruct mesoscale volumes over an order of magnitude larger in linear dimension (≈ 100 μm) than described above, while maintaining a resolution on the order of tens of nm. Using the 3D PFIB-SEM reconstructions, we quantified both micro- and mesoscale distributions of features in commercial SOFC electrodes. Significant variations were observed in the distributions of features over the mesoscale, which impacted distributions of local electrochemical activity throughout the cell. Moreover, gradients in the distributions existed across the entire volume, indicating the possible existence of heterogeneities on the millimeter scale. Despite making observations and performing preliminary statistical analyses, that work did not fully quantify the mesoscale distributions, which we address in this article.

Recently, several reports concerned with microstructural characterization of electrode microstructures in energy conversion devices have attempted to quantify and correlate heterogeneities to cell reliability and durability.[54–60] M. M. Forouzan et al. [57] reported that spatial variations (or heterogeneities) are one of the main factors that exacerbate the degradation of Liion batteries, causing non-uniform currents, temperatures, states of charge, and aging. Degradation or failure events in SOFC electrodes have also been reported to be tied to heterogeneities and to occur locally at certain regions or morphological features (surfaces, TPBs), such as those with high over-potentials.[52,55,61] Most of these works were still focused on microscale volumes, or smaller. Reliability and performance degradation of SOFCs could be impacted by the width of local performance distributions or the tails of those distributions, which are in turn related to the widths or tails of microstructural distributions. However, quantitative characterization and simulation methods capable of investigating the impact of the full microstructural distributions, including the tails, are lacking.

In this work, we combine analysis of multiple physical reconstructions of commercial SOFC electrodes, both anodes and cathodes collected using PFIB-SEM, with a unique set of synthetic microstructures designed to have controlled distributions in particle size and local volume fractions that span the range of physical observations. We reported recently an initial combined analysis of physical and synthetic microstructures,[52] where we showed that the particle size distributions in synthetic microstructures could model micro-scale heterogeneities on the order of 10-15 particle diameters, but not heterogeneities over longer length scales. Here, we develop a complete semi-empirical model that can be used to quantitatively analyze heterogeneities over both the micro- and mesoscales, specifically between the relationship of the mean-squared normalized variance in the volume fraction, $(\frac{\sigma_{\Phi_V}}{\bar{\Phi}_V})^2$, and the mean particle size normalized linear dimension, $\frac{L}{\bar{a}_N}$. The model can be used to relate different terms back to different initial feedstock and processing parameters used in cell fabrication. By comparing multiple physical reconstructions from the same electrode, millimeter scale variations are also quantified and demonstrated to be statistically important. These results will help accelerate the development of reliable and durable low-cost SOFCs by accelerating the design and fabrication of optimal microstructures.

2. Methods

Standard 25 mm anode supported SOFC button cells obtained from a commercial supplier (Materials and Systems Research, Inc. (MSRI), Salt Lake City, UT) were used in this work. We previously reported on microstructural heterogeneities in commercial cells using laboratory nano-CT,[47] synchrotron micro-CT methods,[47] and PFIB-SEM.[51,52] Herein, we report additional 3D microstructure reconstructions of the MSRI cells: two mesoscale cathodes, called C^1 and C^2, and one mesoscale anode, called A^1. The phase compositions of cathode (C) and anode (A) were, respectively, LSM/YSZ/Pore and YSZ/Ni/Pore.

A DualBeam Helios PFIB-SEM (FEI Company, Hillsboro, OR) equipped with the commercial 3D acquisition package "AutoSlice and View" (FEI Company, Hillsboro, OR) was used to collect 3D microstructural datasets. A full description of the sample processing and 3D microstructure acquisition using PFIB-SEM method can be found elsewhere.[51,52] The image resolution was 65 nm in the SEM images and the spacing between 2D images was 65 nm, for all three datasets. Cathode C^1 and anode A^1 were extracted from the same pristine MSRI cell previously studied by Mahbub et al.[51] and Hsu et al.[52] The PFIB-SEM scanned cathode and anode datasets discussed by Hsu et al.[52] are referred to respectively as C^{3*} and A^{2*} in this work. The C^2 cathode was extracted from a different cell from the same manufacturer. The cell from which C^2 was extracted was operated for 1500 hours; this operational time is not expected to cause significant changes to the SOFC cathode microstructure that are observable at ~ 65 nm resolution,[62–65] and we simply focus on quantifying variability between regions of different cells.

To rationalize the origin of heterogeneities measured in the experimental datasets using PFIB-SEM, several types of synthetic microstructures were used. First, the synthetic microstructures reported by Hsu et al.[52], named S-0.34, S-0.40, S-0.50, and S-0.63, were used again in this work. In general the series is denoted as S-$\frac{\sigma_{a_N}}{\bar{a}_N}$, where S indicates a synthetically generated microstructure and the number indicates the mean-normalized standard deviation of the (number-weighted) particle size, $\frac{\sigma_{a_N}}{\bar{a}_N}$. The relevant data from the S-$\frac{\sigma_{a_N}}{\bar{a}_N}$ series are given in Table I under the particle size distribution heading.

Furthermore, a new series of synthetic microstructures were generated to simulate mesoscale volume fraction distributions that might arise from agglomeration in feedstock powders or inks used in processing. To simulate this, a library of microscale synthetic building block microstructures, with a building block edge length of L_{BB}, were generated as before[52] using DREAM.3D (BlueQuartz Software, Springboro, OH) to have different volume fractions of phases with specific particles size distributions identical to the first series: $\frac{\sigma_{a_N}}{\bar{a}_N}$ = 0.34, 0.40, 0.50, or 0.63. Herein we discuss microstructures constructed from cubic building blocks of L_{BB}=12.5 µm (and 6.25 µm) with voxel sizes of 125 nm. Synthetic microstructures in the volume fraction distribution series were generated by assembling a 10 x 10 (20 x 20) array of building blocks from the library, such that the whole domain was 125 x 125 x 12.5 µm^3 and was similar to the PFIB datasets, sampled to obtain a truncated normal distribution with a specific average volume fraction $\bar{\Phi}_V$ and a specific mean-squared normalized variance of the aggregated (volume-weighted) phase fraction, $(\frac{\sigma_{\Phi_V}}{\bar{\Phi}_V})^2_{BB}$ (where BB indicates the term is evaluated at L_{BB}). For all synthetic microstructures described herein, $\bar{\Phi}_V$ was targeted at 0.33 for all phases. The 100 building blocks that attained the target distributions were then stitched together in a random arrangement. This second series of synthetic microstructures are called S-$\frac{\sigma_{a_N}}{\bar{a}_N}$-$(\frac{\sigma_{\Phi_V}}{\bar{\Phi}_V})^2_{BB}$-$L_{BB}$. The properties from the S-$\frac{\sigma_{a_N}}{\bar{a}_N}$-$(\frac{\sigma_{\Phi_V}}{\bar{\Phi}_V})^2_{BB}$-12.5 series are tabulated in Table I under the volume fraction distribution heading.

Custom MATLAB (Mathworks, Natick, MA) and Python codes written in-house were used to quantify morphological and electrochemical parameters in the reconstructed 3D datasets, which include phase fraction, tortuosity, TPB density, and polarization resistance. Details regarding the calculation approach of these parameters is discussed in Epting et al.[47,58] and Hsu et al.[52] Using another set of custom MATLAB codes, the large volume PFIB-SEM datasets (C^1, C^2 and A^1) were sub-divided into small non-overlapping thickness^3 (t^3) sub-volumes which are reasonable to describe local electrochemical activity.[19,21,23,52] For each sub-volume, parameters of interest were calculated and then their distributions in the datasets were quantified. Finally, the distributions of features in cathodes C^1, C^2, and C^{3*}, as well as in anodes A^1 and A^{2*}, were compared to analyze the impact of heterogeneities on cell electrochemistry and performance distributions.

3. Results and Discussion

3.1. Experimental Data

Figures 1a-1c show 3D renderings, of mesoscale rectangular prisms extracted from the large reconstructed and segmented data, of an anode active layer (A^1) and two cathode active layers (C^1 and C^2). [For the cells characterized here, the "active layer" of the electrode refers to the 10-20 μm of electrode that is directly in contact with the dense electrolyte layer.] 3D renderings of the raw datasets are shown in Figure S1 (similar renderings for A^{2*} and C^{3*} are given in Ref. [52]). The dimensions in-plane and the thickness (t) of the anode A^1 are 124 x 70 μm^2 and 9 μm, and of the cathode C^1 {C^2} are 179 x 100 {189 x 130} μm^2 and 10 {11.5} μm respectively. The voxel size and resolution are both 65^3 nm^3, in all data sets, yielding ≈ 2.8 x 10^8, 6.5 x 10^8, and 1.0 x 10^9

voxels in A^1, C^1, and C^2 reconstructions, respectively. These two cathode datasets, to our knowledge, are the largest reported microstructural volumes in the literature with that level of nano-scale resolution. From inspection of Figure 1, it is visually evident that the nature of heterogeneity varies in the three microstructures. The anode A^1 (Fig. 1a) has the most uniform distribution in the color of the rendered solid phases (yellow/red). On the other extreme, the cathode C^2 (Figure 1c) has the least uniform distribution, with large regions of mostly blue or yellow solids. The cathode C^1 (Figure 1b) is in between the others, with smaller regions of individual colors being readily apparent.

One approach to quantifying the heterogeneity in microstructures is a varying sub-volume analysis, as described elsewhere.[47,52] Plots are given in Figure 2 (on a linear scale in 2a and a semi-log scale in 2b) that quantify the variation in volume fractions between sub-volumes of different sizes, specifically of the mean-squared normalized variance of the aggregated (volume-weighted) phase fraction, $(\frac{\sigma_{\Phi_V}}{\bar{\Phi}_V})^2$, for non-overlapping sub-volumes of different mean particle size normalized edge lengths, $\frac{L}{\bar{a}_N}$. Data in Figure 2 include two anodes (triangles), A^1 (black) and A^{2*} (grey), and three cathodes (circles), C^1 (black), C^2 (blue), and C^{3*} (grey), where A^{2*} and C^{3*} are from previously published[52] datasets from the same commercial supplier. The linear plots in Figure 2a clearly shows the micro to mesoscale variabilities existing at smaller and intermediate sub-volume sizes in these electrode reconstructions, while the semi-log plots in Figure 2b gives a better visualization of the variabilities existing at longer length scales. The inset in Figure 2a highlights the anode variability. The anodes are clearly more homogeneous than the cathodes in Figure 2, having much lower $(\frac{\sigma_{\Phi_V}}{\bar{\Phi}_V})^2$ values for nearly all sub-volume sizes. However, above $\frac{L}{\bar{a}_N} \approx 60$, the value for anode, A^{2*}, which became constant above $\frac{L}{\bar{a}_N} \approx 20$, approaches and surpasses those of

C^{3*} and C^1, but remains below C^2. The differences remain similar between each cathode over the whole range, with $(\frac{\sigma_{\Phi_V}}{\bar{\Phi}_V})^2$ values for cathode, C^{3*} being less than those for C^1, which are less than those for C^2. While the anodes mainly have variabilities at smaller and larger sub-volume sizes, variabilities over the microscale, mesoscale, and even longer length scales (existing at smaller, intermediate and larger sub-volume sizes, repsectively) are prominent in the cathodes. The primary question in this paper is: can we model these heterogeneities and relate them back to fundamental processing parameters?

3.2. Particle Size Distribution Effects

Chiu[21] developed a model to describe microstructural heterogeneities assuming all phases in the microstructure have identical sizes and the phases are distributed statistically at random using a binomial distribution. In that model, if one selects n particles that have a probability p of being a specific phase, then the mean is $\bar{\Phi}_{bi} = n(p)$ and the variance is ${\sigma_{\bar{\Phi}_{bi}}}^2 = n(p)(1-p)$. Thus, the mean-squared normalized variance in phase fractions is simply $\left(\frac{\sigma_{\bar{\Phi}_{bi}}}{\bar{\Phi}_{bi}}\right)^2 = \frac{(1-p)}{p}(n)^{-1}$. Following Chiu's model for a monodisperse set of cubic particles of edge length $\bar{a}_N$, then the number of particles n in a cubic volume L is $n = (\frac{L}{\bar{a}_N})^3$. It follows then that the mean-squared normalized variance in phase fractions follows a negative third order power law with respect to the mean particle size normalized edge lengths:

$$\left(\frac{\sigma_{\Phi_V}}{\bar{\Phi}_V}\right)^2 = A(\frac{L}{\bar{a}_N})^{-3} \qquad \textbf{Eq. 1,}$$

where A is a constant related to the statistical distribution; e.g., a binomial distribution has $A = \frac{(1-p)}{p}$ (where p is the volume fraction).

For microstructures that do not conform to the assumptions above, where closed forms of the appropriate statistical distributions are unknown, we have used synthetic microstructures generated with specific heterogeneities to develop quantitative descriptions of physical microstructures.[52,66] We reported previously[52] that the width of the distribution in the particle size used to form synthetic data sets, or more specifically the mean normalized (number-weighted) particle size standard deviation $\frac{\sigma_{a_N}}{\bar{a}_N}$, lead to variability in volume fractions that matched experimental values (for C[3*] and A[2*]) at small micro-scale sub-volume sizes, $\frac{L}{\bar{a}_N} \lesssim 10$.

We reconsidered the four synthetic microstructures[52] that were generated with similar mean volume fractions $\bar{\Phi}_V$ but different target particle size distributions (PSDs), quantified by $\frac{\sigma_{a_N}}{\bar{a}_N}$, to address: does the power law dependence hold for the synthetic data sets? Plots of datapoints for $(\frac{\sigma_{\Phi_V}}{\bar{\Phi}_V})^2$ versus $\frac{L}{\bar{a}_N}$ are given in Figure 3 from synthetic microstructures having $\bar{\Phi}_V$=0.33 and $\frac{\sigma_{a_N}}{\bar{a}_N}$ = 0.34 (red), 0.40 (blue), 0.50 (green), and 0.63 (black), both in linear (3a) and semi-log (3b) scales. The data was then fit to a modified version of Eq. 1, given in Eq.2,

$$(\frac{\sigma_{\Phi_V}}{\bar{\Phi}_V})^2 = \begin{cases} A_{PSD}(\frac{L}{\bar{a}_N})^{-3},\ L < t \\ A_{PSD}(\frac{t}{\bar{a}_N})^{-1}(\frac{L}{\bar{a}_N})^{-2}, L \geq t \end{cases} \qquad \textbf{Eq. 2,}$$

which accounts for the data being non-cubic above the electrode thickness, t, and allowing A to be a fitting parameter, A_{PSD}. The A_{PSD} values of the four synthetics having different polydispersity of particle size are shown in Table II under the model parameters for **S-**$\boldsymbol{\frac{\sigma_{a_N}}{\bar{a}_N}}$ datasets heading. For all $\frac{\sigma_{a_N}}{\bar{a}_N}$ values, the inverse power law of Eq. 2 fits all the data well, as is shown by the similar color solid lines to the datapoints in Figure 3 and is best viewed in the semi-log plot. An interesting outcome of this analysis is that synthetic microstructures can be used to quantify the effects of particle size distributions on volume fraction variations, in lieu of a rigorous mathematical model. The A_{PSD} value for any given microstructure dataset can be modeled simply by quantifying the polydispersity of their particle sizes, $\frac{\sigma_{a_N}}{\bar{a}_N}$, which can be done experimentally, and compare to known A_{PSD} values from synthetic datasets (with similar $\bar{\Phi}_V$ values), establishing exact values through extrapolation/interpolation.

3.3. Quantitative Analysis of Anodes: Micro-scale and Millimeter-Scale Variations

As described before, the anode datasets are more homogeneous than the cathodes over the microscale, and it was previously reported[52] that particle size distributions explains the variability in anode, A^{2*} data well, at lower values of $\frac{L}{\bar{a}_N}$. Heterogeneity analysis plots of $(\frac{\sigma_{\Phi_V}}{\bar{\Phi}_V})^2$ versus $\frac{L}{\bar{a}_N}$ are given in Figure 4, in linear (4a) and semi-log (4b) scales, for A^1 (black) and A^{2*} (gray). The dashed lines given correspond to curves from the modified power law model from Eq. 2. The A_{PSD} value was fixed by experimentally measuring $\frac{\sigma_{a_N}}{\bar{a}_N}$ and using the A_{PSD} value of the similar synthetic data sets described above. The lines fit the data sets extremely well at lower values of $\frac{L}{\bar{a}_N}$, but not at the higher values. At the largest $\frac{L}{\bar{a}_N}$, the $(\frac{\sigma_{\Phi_V}}{\bar{\Phi}_V})^2$ value for the experimental anodes are much larger than those from the synthetic datasets having similar polydispersity of particle size ($\frac{\sigma_{a_N}}{\bar{a}_N}$ = 0.40), by a factor of 3 to 20. This indicates the data sets have some long-range variation in volume fractions, not captured by the homogeneous synthetic model, which also differs between the two anode datasets.

To capture this long-wavelength heterogeneity for any given dataset, a constant term was introduced into Eq. 2., as shown in Eq. 3:

$$(\frac{\sigma_{\Phi_V}}{\bar{\Phi}_V})^2 = \begin{cases} A_{PSD}(\frac{L}{\bar{a}_N})^{-3} + C_{L_m}, \ L < t \\ A_{PSD}(\frac{t}{\bar{a}_N})^{-1}(\frac{L}{\bar{a}_N})^{-2} + C_{L_m}, L \geq t \end{cases} \qquad \textbf{Eq. 3,}$$

where C_{L_m} represents the difference between the value of $(\frac{\sigma_{\Phi_V}}{\bar{\Phi}_V})^2$ in the microstructure dataset at the maximum sub-volume size, L_m, and the value $(\frac{\sigma_{\Phi_V}}{\bar{\Phi}_V})^2$ at L_m computed using Eq. 2 with the same A_{PSD} value. In a most basic sense, C_{L_m} describes the effect of a finite volume in an unknown long wavelength heterogeneity. Curves generated with Eq. 3, using the appropriate value of A_{PSD} from the S-$\frac{\sigma_{a_N}}{\bar{a}_N}$ synthetics and C_{L_m} as described above, are plotted in Figure 4 with solid lines. Following Eq. 3 the curves fit the data over the entire range of $\frac{L}{\bar{a}_N}$ with R-squared value > 0.97. For these anodes, the C_{L_m} term in Eq. 3 quantifies internal gradients in the microstructure over the 100 μm length scale. These gradients are clearly present at levels significantly above a homogeneous electrode, which has $C_{L_m} = 0$. We discuss such longer wavelength variations in a bit more detail later in the text associated with Figure 8. Essentially, the anodes can be readily fit with two constrained parameters, which are constrained by the measured $\frac{\sigma_{a_N}}{\bar{a}_N}$ value, setting A_{PSD}, and the value of $(\frac{\sigma_{\Phi_V}}{\bar{\Phi}_V})^2$ at the largest $\frac{L}{\bar{a}_N}$, fixing C_{L_m}.

3.4. Quantitative Analysis of Cathodes: Mesoscale Heterogeneities

It is clear from Figures 2 and 3, and from prior work, that the experimental cathodes have variations in volume fractions that cannot be explained using only the polydispersity of particle sizes or truncations error from long wavelength gradients, or combinations thereof. Agglomeration can be quantified by both a length scale of the agglomerates and the volume fraction of a given phase within the agglomerates. As such, using approach described in the methods section, synthetic microstructures were generated to simulate agglomeration as local volume fraction variations over a length scale of the building blocks (L_{BB}=12.5 μm), named S-$\frac{\sigma_{a_N}}{\bar{a}_N}$-$(\frac{\sigma_{\Phi_V}}{\bar{\Phi}_V})^2_{BB}$-12.5 microstructures. 3D renderings of two synthetic microstructures in the volume fraction distribution series are given in Figure 5, for (a) S-0.40-4.5 x10^{-2}-12.5 and (b) S-0.40-3.0x10^{-1}-12.5; they are colored similarly to the cathode microstructures in Figure 1. (More renderings of other S-$\frac{\sigma_{a_N}}{\bar{a}_N}$-$(\frac{\sigma_{\Phi_V}}{\bar{\Phi}_V})^2_{BB}$-12.5 microstructures are given in the SI. Note that the S-0.40-3.6x10^{-5}-12.5 microstructure, in Figure S5, is similar to the S-0.40 one, just generated with 100 statistically similar S-0.40 building blocks, its $(\frac{\sigma_{\Phi_V}}{\bar{\Phi}_V})^2_{BB}$ is effectively zero). The S-0.40-4.5x10^{-2}-12.5 and S-0.40-3.0x10^{-1}-12.5 microstructures have two obvious features. First, there are significant local clusters reminiscent of those observed in the cathodes of Figure 1. Second, the interfaces of the building blocks are clearly evident (especially in the more heterogeneous one), a result of the random assignment of identically sized cubic building blocks. While the latter feature is clearly different from the experimental datasets, we have found previously[52] that the stitched microstructure is similar enough to use as a tool for quantitative comparisons of heterogeneities.

Heterogeneity analysis plots of $(\frac{\sigma_{\Phi_V}}{\bar{\Phi}_V})^2$ versus $\frac{L}{\bar{a}_N}$ are given in Figure 6, in linear (6a) and semi-log (6b) scales, for all of the S-0.40-$(\frac{\sigma_{\Phi_V}}{\bar{\Phi}_V})^2_{BB}$-12.5 synthetic microstructures. Similar plots for other S-$\frac{\sigma_{a_N}}{\bar{a}_N}$-$(\frac{\sigma_{\Phi_V}}{\bar{\Phi}_V})^2_{BB}$-12.5 microstructures are given in the SI). It should be noted that data points at values where $\frac{L}{\bar{a}_N}$ is an integer fraction of $\frac{L_{BB}}{\bar{a}_N}$ were left off of the plots, as they lead to points lying on a distinct curve owing to the absence of stitching artifacts (and such curves have fewer overall points than those shown). Considering Figure 6a and 6b (with more shown in S6-S8 a and b), it is clear that the new series of synthetic microstructures, having significant local volume fraction variations, do exhibit up to three to four orders of magnitude increase in the variability across the entire mesoscale range (among intermediate sub-volume sizes), as well as a smaller increase in the microscale range. The results from the S-$\frac{\sigma_{a_N}}{\bar{a}_N}$-$(\frac{\sigma_{\Phi_V}}{\bar{\Phi}_V})^2_{BB}$-12.5 synthetic microstructures are qualitatively similar to the experimental cathodes, indicating this type of agglomeration is a likely cause of the mesoscale variability in phase fractions. The question remains: can the variability be quantified?

As a starting point, the heterogeneity analysis data of the S-$\frac{\sigma_{a_N}}{\bar{a}_N}$-$(\frac{\sigma_{\Phi_V}}{\bar{\Phi}_V})^2_{BB}$-12.5 synthetic microstructures were fit with Eq. 3, where the A_{PSD} value was set based on the $\frac{\sigma_{a_N}}{\bar{a}_N}$ of synthetics, and the C_{L_m} value was determined as described above. Those fits are shown in Figure 6c and 6d for all of the S-0.40-$(\frac{\sigma_{\Phi_V}}{\bar{\Phi}_V})^2_{BB}$-12.5 synthetic microstructures (similar plots for other S-$\frac{\sigma_{a_N}}{\bar{a}_N}$-$(\frac{\sigma_{\Phi_V}}{\bar{\Phi}_V})^2_{BB}$-12.5 microstructures are given in the SI in Figure S6-S8 c and d). Such a curve fits the S-0.40-3.6x10^{-5}-12.5 data well, as expected. As $(\frac{\sigma_{\Phi_V}}{\bar{\Phi}_V})^2_{BB}$ increases slightly from 3.6x10^{-5} (target $(\frac{\sigma_{\Phi_V}}{\bar{\Phi}_V})^2_{BB}$ value of 0.000), the curves are reasonable fits to the micro-scale and larger $\frac{L}{\bar{a}_N}$ values, but begin to deviate in central region of the mesoscale. As $(\frac{\sigma_{\Phi_V}}{\bar{\Phi}_V})^2_{BB}$ increases further, more significant deviations occur in the mesoscale and large deviations also occur in the microscale. This additional heterogeneity cannot be captured by Eq. 3. At the largest $(\frac{\sigma_{\Phi_V}}{\bar{\Phi}_V})^2_{BB}$ values, only the last point is well fit by the C_{L_m} term designed to capture it. It should be noted that the value of C_{L_m} is much larger in the S-$\frac{\sigma_{a_N}}{\bar{a}_N}$-$(\frac{\sigma_{\Phi_V}}{\bar{\Phi}_V})^2_{BB}$-12.5 series of synthetics, indicating a significant heterogeneity is introduced in the microstructure across the entire space of $\frac{L}{\bar{a}_N}$ as compared to the S-$\frac{\sigma_{a_N}}{\bar{a}_N}$ synthetics, particularly when $(\frac{\sigma_{\Phi_V}}{\bar{\Phi}_V})^2_{BB}$ is large.

To quantify the intermediate scale heterogeneities, we need to incorporate at least one more term in the model that quantifies local volume fraction variations to duplicate agglomeration behavior. The synthetic series S-$\frac{\sigma_{a_N}}{\bar{a}_N}$-$(\frac{\sigma_{\Phi_V}}{\bar{\Phi}_V})^2_{BB}$-12.5, which incorporates local volume fractions, was populated statistically using a truncated normal distribution from cubic building blocks of length L_{BB} to have a normalized variance of $(\frac{\sigma_{\Phi_V}}{\bar{\Phi}_V})^2_{BB}$ (evaluated at L_{BB}). Thus, we might expect the residual of the Eq. 3 fit to the synthetic S-$\frac{\sigma_{a_N}}{\bar{a}_N}$-$(\frac{\sigma_{\Phi_V}}{\bar{\Phi}_V})^2_{BB}$-12.5 data points to follow an exponential decay of the form $y = Ae^{-Bx}$. Adding such a term to Eq. 3 yields Eq. 4:

$$(\frac{\sigma_{\Phi_V}}{\bar{\Phi}_V})^2 = \begin{cases} A_{PSD}(\frac{L}{\bar{a}_N})^{-3} + A_{VFD}e^{-B_{VFD}\frac{L}{\bar{a}_N}} + C_{L_m},\ L < t \\ A_{PSD}(\frac{t}{\bar{a}_N})^{-1}(\frac{L}{\bar{a}_N})^{-2} + A_{VFD}e^{-B_{VFD}\frac{L}{\bar{a}_N}} + C_{L_m}, L \geq t \end{cases} \quad \textbf{Eq. 4,}$$

where the variables A_{VFD} and B_{VFD}^{-1} terms describe, respectively, the magnitude of the variation in local VF and the building block size over which the variation exists. This is our basic goal, to quantify the length scale and the magnitude of local volume fraction variations, and the exponential term readily describes these. Specifically, we would expect $A_{VFD} = e\left(\frac{\sigma_{\Phi_V}}{\bar{\Phi}_V}\right)^2_{BB}$ and $B_{VFD} = \frac{\bar{a}_N}{L_{BB}}$, if the exponential function was the only term in Eq. 4. In this case, C_{L_m} again represents the difference between the value of $(\frac{\sigma_{\Phi_V}}{\bar{\Phi}_V})^2$ in the microstructure dataset at the maximum sub-volume size, L_m, and the value $(\frac{\sigma_{\Phi_V}}{\bar{\Phi}_V})^2$ at L_m computed for the first terms in Eq. 4, using the same A_{PSD} value. In practice, the first two terms are generally smaller than the gradient or finite volume effects, and the term can simply be approximated as the value of $(\frac{\sigma_{\Phi_V}}{\bar{\Phi}_V})^2$ in the microstructure dataset at the maximum sub-volume size analyzed, L_m.

This semi-empirical model is found to describe heterogeneities of all length scales in the synthetic microstructures of Figure 6 reasonably well, as is shown by the similar color dashed lines in the Figure 6e and 6f (also see Figure S6-S8 c and d for the other synthetic microstructures), with fit values given in Table II under the model parameters for S-0.40-$(\frac{\sigma_{\Phi_V}}{\bar{\Phi}_V})^2_{BB}$-$L_{BB}$ datasets heading. If we compare the fit values for A_{VFD} and B_{VFD} to the $e\left(\frac{\sigma_{\Phi_V}}{\bar{\Phi}_V}\right)^2_{BB}$ and $\frac{\bar{a}_N}{L_{BB}}$ values, there is good agreement. In other words, the exponential fit returns the expected value for the length scale and the magnitude of local volume fraction variations built into the synthetics. Thus, combining the analysis of both the S-$\frac{\sigma_{a_N}}{\bar{a}_N}$ and the S-$\frac{\sigma_{a_N}}{\bar{a}_N}$-$(\frac{\sigma_{\Phi_V}}{\bar{\Phi}_V})^2_{BB}$-$L_{BB}$ series of microstructures, leads to a high confidence that Eq. 4 yields an accurate quantification of the micro- and mesoscale variations. To review the procedure for quantifying heterogeneities using Eq. 4: $\frac{\sigma_{a_N}}{\bar{a}_N}$ is measured experimentally; A_{PSD} is fixed (it is a constrained parameter) to the value fitted to the appropriate S-$\frac{\sigma_{a_N}}{\bar{a}_N}$ series; the C_{L_m} value is fixed (it is a constrained parameter) to the value on the curve at the maximum $\frac{\bar{a}_N}{L_{BB}}$ (or the difference between that value and the value of the appropriate synthetic at the same $\frac{\bar{a}_N}{L_{BB}}$); and finally A_{VFD} and B_{VFD} are fitted (these are the two fitting parameters) by a least squares method to the data using Eq. 4. Following this procedure using the synthetic microstructures, the fitted A_{VFD} and B_{VFD} values reflect the input values of $\left(\frac{\sigma_{\Phi_V}}{\bar{\Phi}_V}\right)^2_{BB}$ and L_{BB}.

We next used the model given in Eq. 4 to quantify the heterogeneities in the experimental cathodes. In Figure 7, mean-squared normalized variance of the aggregated phase fraction, $\left(\frac{\sigma_{\Phi_V}}{\bar{\Phi}_V}\right)^2$, is plotted in linear (a) and semi-log (b) scales, as a function of the mean particle size normalized edge lengths, $\frac{L}{\bar{a}_N}$ for the cathodes C^1 (black), C^2 (blue), and C^{3*} (gray). Fits to the data with Eq. 4

are shown by similarly colored curved lines, and fit values for A_{PSD}, A_{VFD}, B_{VFD}, and C_{L_m} are given in Table III. The curves from Eq. 4 fit the data very well (R-squared value > 0.98), indicating the model quantitatively captures heterogeneities over all length scales in the experimental electrodes with good accuracy. The values of A_{VFD} are approximately 4 x10^{-2} to 5 x10^{-2} for all cathodes, which are most similar to the S-$\frac{\sigma_{a_N}}{\bar{a}_N}$-4.5 x$10^{-2}$-12.5 data sets. The value of $\frac{1}{B_{VFD}}$ represents the normalized length scale of the heterogeneity, and it varies from 9 to 18. The $\frac{1}{B_{VFD}}$ value is 17.9 for the S-0.40-4.5 x10^{-2}-12.5 data set. In fact, the values for S-0.40-4.5 x10^{-2}-12.5 are reasonably close to the cathode C^2 across all parameters.

As observed for the anodes before, in Table III we notice that the C_{L_m} terms for the experimental cathodes are also much higher than what is expected due to only truncation error in a synthetic dataset having similar polydispersity of particle size (or σ_{a_N} / $\bar{a}_N$ value) in Table II. This means, similar to anodes, there exist long wavelength gradients in the cathode datasets as well and the high C_{L_m} values indicate that, this gradient is much more prominent in the cathodes than in anodes.

3.5 Long Wavelength Heterogeneities

Previously, we reported the existence of long wavelength variations in anode, A^{2*} and cathode, C^{3*} using spatial maps. [52] (Similar maps for the new datasets have been discussed in SI in Figure S2 and S3). To explore the long wavelength variations in the electrodes in more details, in Figure 8 we compare the mesoscale distributions of ICP volume fraction measured in the t^3 partitions of anodes A^1 and A^{2*} (Figure: 8a) and cathodes C^1 and C^{3*} (Figure: 8b). These two anode and cathode PFIB scans are extracted from the same cell, simply separated by a fraction of a millimeter (0.1-0.4 mm) in either electrode. Interestingly, the distributions from the two anodes, as well as from the two cathodes, have different means that are separated by almost four standard deviations (which are similar for both distributions), leading to distributions that have almost no significant overlap. Similar results were observed when the volume fraction distributions of other phases in anodes A^1 and A^{2*} and cathodes C^1 and C^{3*} are compared (See Figure S4 for details, similar distributions from cathode, C^2 have also been incorporated in SI).

Even though these anodes appear relatively more homogeneous on the microscale than the cathodes, being built from particles having relatively narrow size distributions of $\frac{\sigma_{a_N}}{\bar{a}_N} = 0.40$, they also exhibit very long wavelength variations in the local phase fractions. The latter is significant enough to result in two relatively large PFIB sub-volumes having no statistical overlap in volume fraction distributions amongst t^3 sub-volumes, though spatially separated by only fractions of millimeters. This longer wavelength variation presents itself in the PFIB data as a gradient, captured locally by the C_{L_m} term in Eq. 3 and Eq. 4. This type of variation indicates the phases are well mixed from a local perspective, but the entire electrode has statistically relevant variations throughout. This impacts the distribution of local performance, as described below, but also makes it difficult to explore time dependent phenomena between cathodes or anodes if PFIB pillars on any given cathode or anode are not identical. One of the challenging consequences of such variations is that it is difficult to assess time-dependent variability between similar electrodes when the initial electrodes contain statistically non-overlapping regions themselves.

3.6 Impact of Heterogeneities on cell Performance Distributions

Thus far we have primarily focused on microstructural heterogeneities in the volume fraction distribution, but other metrics are also important to transport and reaction properties, including the interconnectivity of the different phases that affects tortuosity and triple phase boundary densities.

Figure 9 a-b compares the mesoscale distributions of ECP tortuosity factor and TPB density measured from all non-overlapping t^3 μm^3 sub-volumes of cathodes and anodes (more are given in the SI in Figures S9, for the ICP and GPP). In these figures, the distributions of features from cathodes C^1 and C^2 and anode A^1 (reported herein) have also been compared with previously published[52] similar distributions from cathode C^{3*} and anode A^{2*}. It should be noted that t^3 sub-volumes in the anodes (cathodes) have edge length equal to 13-15 (20-28) times their average particle size: $\frac{t}{\bar{a}_N} = 13 - 15$ (20-28) for anodes (cathodes). Thus, the relative volume (with respect to particle volume) over which features were averaged in the cathode was much greater than in the anodes. In each of these figures, the first block compares the distributions of same features in the three cathodes— C^1 (black), C^2 (blue), and C^{3*} (gray)— and the second block compares their distributions in anodes— A^1 (black) and A^{2*} (gray). As with the volume fraction distributions discussed above (Figure 8) for regions of the same cell from different location, the mesoscale distribution tortuosity and TPB density are distinctly different from regions of the same cell from different locations. Thus, microstructural heterogeneity in these electrodes also impacted the distribution of higher order metrics of network topology / connectivity. This applies to the tails of the distributions too, as the distributions in the cathodes are more skewed with longer tails than those in the anodes for the tortuosity and TPB density metrics.

The local polarization resistance R_p, an indicator of local electrochemical properties, was computed by taking the microstructural parameters as input into an effective medium theory (EMT) model known as the modified Tanner–Fung–Virkar (*m*-TFV) model.[31,45,52,67] The details regarding instantiation of the model are described elsewhere.[52] Figure 9c plots the distribution of polarization resistance R_P^C in cathodes, C^1, C^2, and C^{3*}, and Figure 9d plots the distribution of R_P^A in anodes, A^1 and A^{2*}. These figures show that, there are significant tails towards the larger R_P^C

values in the distributions extracted from the cathode datasets and towards lower R_P^A values in the distributions from the anodes, with some micro-scale volumes having R_p values more than twice the mean. These distributions confirm that, both in cathode and anode microstructures, there are significant microscale t^3 μm^3 that are operating well outside the average values and that vary significantly over the mesoscale and millimeter scales.

Figure 9 c and 9 d also show that, there is ≈ 11, 13 and 6 % variability in performance among the microscale volumes within the cathodes, C^1, C^2, and C^{3*} respectively and ≈ 4% variability within anodes, A^1 and A^{2*}. Furthermore, there exist ≈ 16% variation in mesoscale performance between cathodes, C^1 and C^{3*} with C^2 and ≈ 7 % variation the between mesoscale anodes, A^1 and A^{2*}. Considering that 0.2% per 1000 hours of operation is an acceptable degradation rate for long term cell performance over 50,000 hours,[5] any local variation in performance of ≈ 10% is clearly significant. For example, a performance variation of as low as 1 % between two regions, has the same effect where one region has been operated 5000 more hours than the other. As such, the variability within and as well as among the reconstructions reported here indicate that certain microscale or even mesoscale regions in these cells can be considered as performance failures when compared to the regions with maximum cell performance. Importantly, these performance variations are directly the result of the microstructural heterogeneities, which can be quantified and related to particle size distributions in feedstocks, as well as volume fraction variations associated with agglomeration and long-range mixing stability processing batches (e.g., inks).

Such variations not only impact local cell performance and cell reliability, but can impact negatively the long-term performance if they accelerte degradation phenomenon related to the overpotential.[47,52,54,55,59,60] In other words, heterogeneous cells may also degrade faster than homogeneous cells. To investigate this, an in-house multiphysics model called DREAM-SOFC, [68,69] was used to model the effect that microstructural heterogeneity will have on performance. DREAM-SOFC was previously used to predict performance degradation due to coarsening of SOFC microstructures.[70] 3D distributions of microstructural parameters were obtained from synthetically generated S-0.5-$(\frac{\sigma_{\Phi_V}}{\bar{\Phi}_V})^2_{BB}$-6.25 microstructures (details on generating the synthetics have already been discussed in the method section), where the polydispersity of particle size was similar to the experimental cathode reconstructions and the volume fraction distributions $(\frac{\sigma_{\Phi_V}}{\bar{\Phi}_V})^2_{BB}$ were varied to simulate heterogeneities observed in the cathodes (believed to be associated with agglomeration). The microstructural parameters were used to describe the active layer in multiphysics performance simulation of an LSM half-cell with domain and boundary conditions applied as in [71] with model parameters like those applied in [70]. By calculating the current density for incrementally increasing applied voltages, V-I curves were produced for S-0.5-$(\frac{\sigma_{\Phi_V}}{\bar{\Phi}_V})^2_{BB}$-6.25 datasets, as is shown in Figure 10a. From such data, the overpotential required to operate at a given current density was extracted, and is plotted for two current densities in Figure 10b as a function of the logarithm of the local volume fraction variability (log $(\frac{\sigma_{\Phi_V}}{\bar{\Phi}_V})^2_{BB}$). These figures show that the voltage drop (or the overpotential) across the cathode increases significantly with increasing heterogeneity (at a given current density); further, there is a linear correlation (in the semi-log plot) of Figure 10b, where the slope increases with increasing current density. These results indicate that there is a relatively large overpotential increase associated with heterogeneous cell microstructures, when compared to their homogeneous analogues. Thus, the combination of wider distribution of local performance and the resulting lower effective performance gives an indication that heterogeneous cells underperform and will be prone to faster degradation (considering overpotential driven degradation modes) relative to the homogenously mixed ones. Thus,

quantification of the multi-length scale variations is important to production of reliable and durable SOFCs at reasonable costs.

3.7 Summary

Prior microstructural research with nanoscale resolution of phases in electrodes has successfully characterized and correlated microstructural properties to local electrochemical performance,[47,54,55,59,60] but could not assess variability in microscale properties across devices. This work combined analysis on multiple PFIB-SEM scanned electrode microstructure reconstructions from the same cells, as well as different cells of the same manufacturer, which allowed quantifying heterogeneities over length scale that has not been studied before. To model the possible origins of such heterogeneities, synthetic microstructures of sufficiently large volumes were generated having different particle size distributions (*PSDs*) and local volume fraction distributions (*VFDs*), such that they span the range of heterogeneities quantified in experimental microstructures. By coupling analysis on the experimental and synthetic microstructures, a semi-empirical model was developed to include a negative power law term modeling *PSDs*, a negative exponential term modeling local VFDs (agglomeration), and a constant term modeling poor mixing/gradients over longer ranges. These volume fraction variations, in turn, impact multiscale variations of cell electrochemistry and performance parameters, as shown using well established effective medium theory models. Taken altogether, this approach will accelerate our understanding of processing-structure-performance relationships that are essential for the development of reliable, durable, low-cost SOFCs. Similar approaches could guide the understanding and optimization of other functional composite or porous materials, including other fuel cell or battery electrodes.

4. Conclusion

Combining multiple PFIB-SEM scanned reconstructions, heterogeneities in complex SOFC electrode microstructures over multiple length scales were quantified. By coupling analysis with synthetic microstructures that are generated to have the same range of heterogeneities as the experimental microstructures, a semi empirical model was developed that can quantitatively rationalize the origin of such heterogeneities in terms of feedstock and processing parameters. Specifically, the semi-empirical model accounts for particle/pore size distributions, agglomeration of materials, and long-scale variations that may arise from processing methods. Quantifying the impact of heterogeneities on cell electrochemistry and performance distributions demonstrated the importance of characterizing heterogeneities for improving the cell reliability and durability. In a broader sense, this work offers a path to quantify multiscale heterogeneities in complex composite microstructures, analyze their impact on property or performance distributions and to quantitatively rationalize their origins, ultimately allowing researchers to improve the performance and durability of such functional materials.

Data Availability

The data used in this paper is hosted on the National Energy Technology Laboratory's Energy Data Exchange server at the following URL:

https://edx.netl.doe.gov/dataset/heterogeneous-sofc-electrodes-from-jecs-paper-2019

Acknowledgements

The authors acknowledge use of the Materials Characterization Facility at Carnegie Mellon University supported by grant MCF-677785. We thank Shiwoo Lee at NETL, Morgantown for epoxy infiltration of the button cells. This work was performed in support of the National Energy Technology Laboratory's ongoing research under the RSS contract 89243318CFE000003. This project was supported in part by an appointment to the Internship/Research Participation Program at the National Energy Technology Laboratory, U.S. Department of Energy, administered by the Oak Ridge Institute for Science and Education. The plasma FIB was acquired using support from the National Science Foundation under MRI grant DMR 1428480. This work was also supported in part by a CMU ProSEED/EQT Foundation Grant. **Disclaimer.** This work was funded by the Department of Energy, National Energy Technology Laboratory, an agency of the United States Government, through a support contract with Leidos Research Support Team (LRST). Neither the United States Government nor any agency thereof, nor any of their employees, nor LRTS, nor any of their employees, makes any warranty, expressed or implied, or assumes any legal liability or responsibility for the accuracy, completeness, or usefulness of any information, apparatus, product, or process disclosed, or represents that its use would not infringe privately owned rights. Reference herein to any specific commercial product, process, or service by trade name, trademark, manufacturer, or otherwise, does not necessarily constitute or imply its endorsement, recommendation, or favoring by the United States Government or any agency thereof. The views and opinions of authors expressed herein do not necessarily state or reflect those of the United States Government or any agency thereof.

References:

1. H. Zhang, X. Yu, and P. V Braun, *Nat. Nanotechnol.*, **6**, 277–281 (2011).

2. S. J. Dillon and K. Sun, *Curr. Opin. Solid State Mater. Sci.*, **16**, 153–162 (2012).

3. N. Q. Minh and T. Takahshi, *Comp. Educ.*, **49**, 374–387 (2013).

4. W. G. C. Ryan O’hayre, Suk-Won Cha, *Wiley*, 603 (2016).

5. I. EG&G Technical Services, *Fuel Cell*, **7 Edition**, 1–352 (2004).

6. S. B. A. ATKINSON, J. T. S. I. R. J. GORTE, M. M. A. J. MCEVOY, and S. C. S. J.VOHS, *Int. J. Hydrogen Energy*, **36**, 7251–7256 (2011).

7. A. B. Stambouli and E. Traversa, *Renew. Sustain. Energy Rev.*, **6**, 433–455 (2002).

8. S. P. S. Badwal and K. Foger, *Ceram. Int.*, **22**, 257–265 (1996).

9. A. V Virkar, J. Chen, C. W. Tanner, and J. Kim, **131**, 189–198 (2000).

10. J. R. Wilson et al., *Nat. Mater.*, **5**, 541–544 (2006).

11. Y. Yi, A. D. Rao, J. Brouwer, and G. S. Samuelsen, *J. Power Sources*, **144**, 67–76 (2005).

12. P. R. Shearing, D. J. L. Brett, and N. P. Brandon, *Int. Mater. Rev.*, **55**, 347–363 (2010).

13. K. Matsuzaki, N. Shikazono, and N. Kasagi, *J. Power Sources*, **196**, 3073–3082 (2011).

14. M. Kishimoto, H. Iwai, M. Saito, and H. Yoshida, *J. Power Sources*, **196**, 4555–4563 (2011).

15. D. Kanno, N. Shikazono, N. Takagi, K. Matsuzaki, and N. Kasagi, *Electrochim. Acta*, **56**, 4015–4021 (2011).

16. J. R. Wilson, J. S. Cronin, and S. A. Barnett, *Scr. Mater.*, **65**, 67–72 (2011).

17. J. R. Wilson et al., *J. Power Sources*, **195**, 1829–1840 (2010).

18. A. Bertei and C. Nicolella, *J. Power Sources*, **196**, 9429–9436 (2011).

19. J. Joos, M. Ender, T. Carraro, A. Weber, and E. Ivers-Tiffée, *Electrochim. Acta*, **82**, 268–276

(2012).

20. G. J. Nelson et al., *Acta Mater.*, **60**, 3491–3500 (2012).

21. W. M. Harris and W. K. S. Chiu, *J. Power Sources*, **282**, 552–561 (2015).

22. M. E. Lynch, D. S. Mebane, Y. Liu, and M. Liu, *J. Electrochem. Soc.*, **155**, B635 (2008).

23. W. M. Harris and W. K. S. Chiu, *J. Power Sources*, **282**, 622–629 (2015).

24. H. Yokokawa, H. Tu, B. Iwanschitz, and A. Mai, *J. Power Sources*, **182**, 400–412 (2008).

25. D. Yan et al., *Appl. Energy*, **175**, 414–420 (2016).

26. D. Kennouche et al., *Acta Mater.*, **103**, 204–210 (2016).

27. K. Yakal-Kremski, J. S. Cronin, Y. C. K. Chen-Wiegart, J. Wang, and S. A. Barnett, *Fuel Cells*, **13**, 449–454 (2013).

28. D. Kennouche, Y. -c. K. Chen-Wiegart, J. S. Cronin, J. Wang, and S. A. Barnett, *J. Electrochem. Soc.*, **160**, F1293–F1304 (2013).

29. P. R. Shearing, J. Golbert, R. J. Chater, and N. P. Brandon, *Chem. Eng. Sci.*, **64**, 3928–3933 (2009).

30. P. R. Shearing et al., *J. Power Sources*, **195**, 4804–4810 (2010).

31. N. Vivet et al., *J. Power Sources*, **196**, 7541–7549 (2011).

32. J. S. Cronin, J. R. Wilson, and S. A. Barnett, *J. Power Sources*, **196**, 2640–2643 (2011).

33. D. Gostovic, J. R. Smith, D. P. Kundinger, K. S. Jones, and E. D. Wachsman, 214–217 (2007).

34. H. Iwai et al., *J. Power Sources*, **195**, 955–961 (2010).

35. B. Rüger et al., *ECS Trans.*, **25**, 1211–1220 (2009).

36. Z. Jiao, N. Shikazono, and N. Kasagi, **159**, 285–291 (2012).

37. G. J. Nelson et al., *Electrochem. commun.*, **13**, 586–589 (2011).

38. E. A. Wargo, T. Kotaka, Y. Tabuchi, and E. C. Kumbur, *J. Power Sources*, **241**, 608–618 (2013).

39. P. R. Shearing, J. Gelb, and N. Brandon, *ECS Trans.* , **19**, 51–57 (2009).

40. J. Laurencin et al., *J. Power Sources*, **198**, 182–189 (2012).

41. V. Julie et al., *J. Power Sources*, **243**, 841–849 (2013).

42. A. Tkachuk et al., **222**, 650–655 (2007).

43. P. S. Jørgensen, K. Yakal-kremski, J. Wilson, J. R. Bowen, and S. Barnett, *J. Power Sources*, **261**, 198–205 (2014).

44. P. R. Shearing et al., *Electrochem. Solid-State Lett.*, **14**, B117 (2011).

45. J. S. Cronin, Y. C. K. Chen-Wiegart, J. Wang, and S. A. Barnett, *J. Power Sources*, **233**, 174–179 (2013).

46. Y. C. Karen Chen-Wiegart et al., *J. Power Sources*, **218**, 348–351 (2012).

47. W. K. Epting et al., *J. Am. Ceram. Soc.*, **100**, 2232–2242 (2017).

48. Y. Guan et al., **3**, 885112 (2013).

49. K. N. Grew et al., (2010).

50. S. J. Dillon et al., *J. Am. Ceram. Soc.*, **94**, 4045–4051 (2011).

51. R. Mahbub et al., *ECS Trans.*, **78**, 2159–2170 (2017).

52. T. Hsu et al., *J. Power Sources*, **386**, 1–9 (2018).

53. T. Yang et al., *Int. J. Hydrogen Energy*, **43**, 15445–15456 (2018).

54. M. Krumpelt et al., 228–233 (2010).

55. T. A. Prokop, K. Berent, H. Iwai, J. S. Szmyd, and G. Brus, *Int. J. Hydrogen Energy*, **43**, 10016–10030 (2018).

56. Z. Fishman, J. Hinebaugh, and A. Bazylak, 1643–1650 (2010).

57. M. M. Forouzan, B. A. Mazzeo, and D. R. Wheeler, **165** (2018).

58. W. K. Epting, J. Gelb, and S. Litster, *Adv. Funct. Mater.*, **22**, 555–560 (2012).

59. A. Bertei, V. Yu, F. Tariq, and N. P. Brandon, **396**, 246–256 (2018).

60. S. Wang, T. a. Cruse, M. Krumpelt, B. J. Ingram, and P. a. Salvador, *J. Electrochem. Soc.*, **158**, B152 (2011).

61. T. Hsu et al., *ECS Trans.*, **78**, 2711–2722 (2017).

62. H. Wang et al., *J. Electrochem. Soc.*, **163**, F581–F585 (2016).

63. L. C. Baqué, P. S. Jørgensen, K. V. Hansen, and M. Søgaard, *ECS Trans.* , **57**, 2027–2036 (2013) t.

64. L. C. Baque, P. S. Jorgensen, W. Zhang, K. V. Hansen, and M. Sogaard, *J. Electrochem. Soc.*, **162**, F971–F981 (2015).

65. A. Zekri et al., *J. Electrochem. Soc.*, **164**, F1385–F1391 (2017).

66. S. Mandal, J. Lao, S. Donegan, and A. D. Rollett, *Scr. Mater.*, **146**, 128–132 (2018).

67. W. Tanner, Kuan-Zong Fungm and A. V. V. Cameron, *J. Electrochem. Soc*, **144**, 21–30 (1997).

68. S. R. Pakalapati and I. Celik, *Ph.D. Diss.*, West Virginia University, (2006).

69. F. Elizalde-Blancas, *Ph.D. Diss.*, West Virginia University, (2009).

70. J. Mason, I. Celik, S. Lee, H. Abernathy, and G. Hackett, *J. Electrochem. Soc.*, **165**, F64–F74 (2018).

71. J. Mason, I. Celik, H. Abernathy, and G. Hackett, *ECS Trans.*, **78**, 2855–2864 (2017).

Figures

Figure 1. Rendered images of the segmented data for (a) the active anode, A^1, (b) the active cathode, C^1, and (c) the active cathode, C^2. In each, yellow represents the ICP and red {blue} represents the ECP in the anode {cathodes}. In all images, the segmented pore regions have been rendered as transparent.

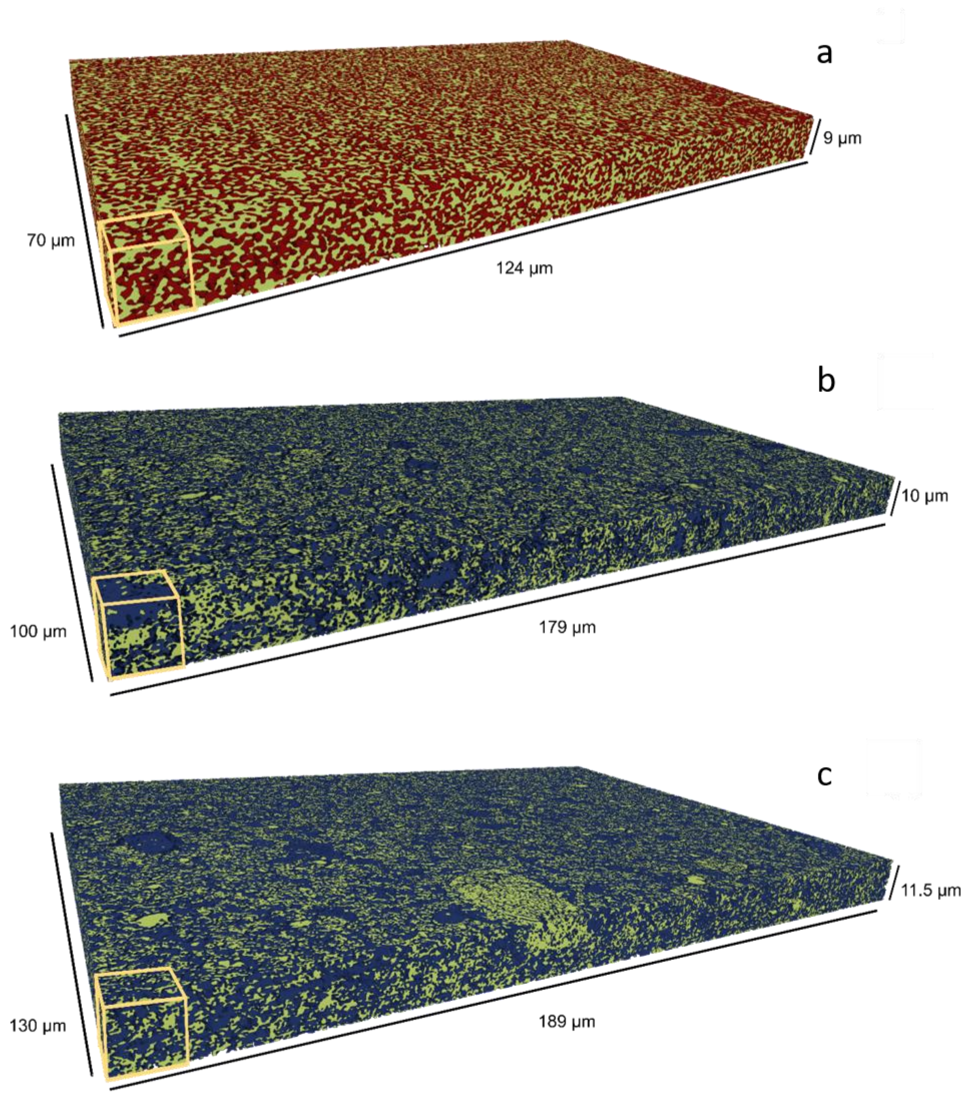

Figure 2. Mean-squared normalized variance of the aggregated phase fraction, $\left(\frac{\sigma_{\Phi_V}}{\bar{\Phi}_V}\right)^2$, plotted in linear (a) and semi-log (b) scales, as a function of the mean particle size normalized edge lengths, $\frac{L}{\bar{a}_N}$. Data points are given for experimental anodes (triangles)— A^1 (black) and A^{2*} (gray)— and cathodes (circles)— C^1 (black), C^2 (blue), and C^{3*} (grey). Lines are meant as guides to the eye.

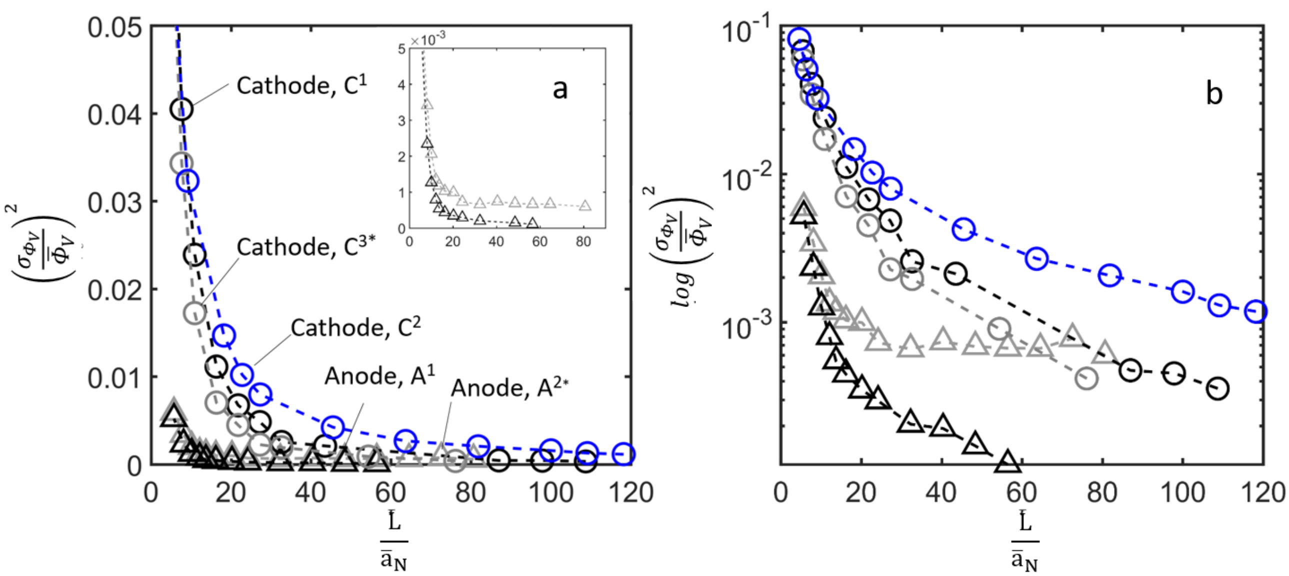

Figure 3. Mean-squared normalized variance of the aggregated phase fraction, $\left(\frac{\sigma_{\Phi_V}}{\bar{\Phi}_V}\right)^2$, plotted in linear (a) and semi-log (b) scales, as a function of the mean particle size normalized edge lengths, $\frac{L}{\bar{a}_N}$. Data points are shown for synthetic S-$\frac{\sigma_{a_N}}{\bar{a}_N}$ microstructures simulating different particle size distributions: S-0.34 (red), S-0.40 (blue), S-0.50 (green), and S-0.63(black). Fits to the data with the power law model of Eq. 2 are shown by similar color curved lines (fit values for A_{PSD} are given in Table II).

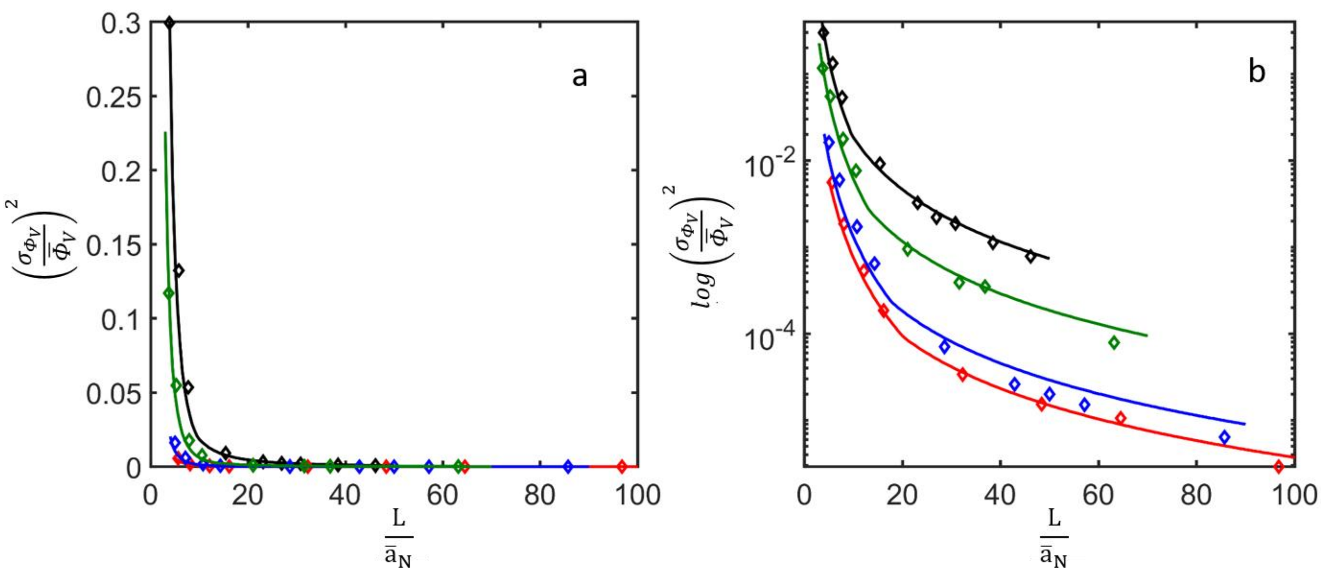

Figure 4. Mean-squared normalized variance of the aggregated phase fraction, $\left(\frac{\sigma_{\Phi_V}}{\bar{\Phi}_V}\right)^2$, plotted in linear (a) and semi-log (b) scales, as a function of the mean particle size normalized edge lengths, $\frac{L}{\bar{a}_N}$. Data points are shown for experimental anodes: Fits to the data with the power law model of Eq. 3 are shown by similar color curved lines (fit values for A_{PSD} and C_{L_m} are given in Table III), with dashed curves showing the fit before incorporating the C_{L_m} term

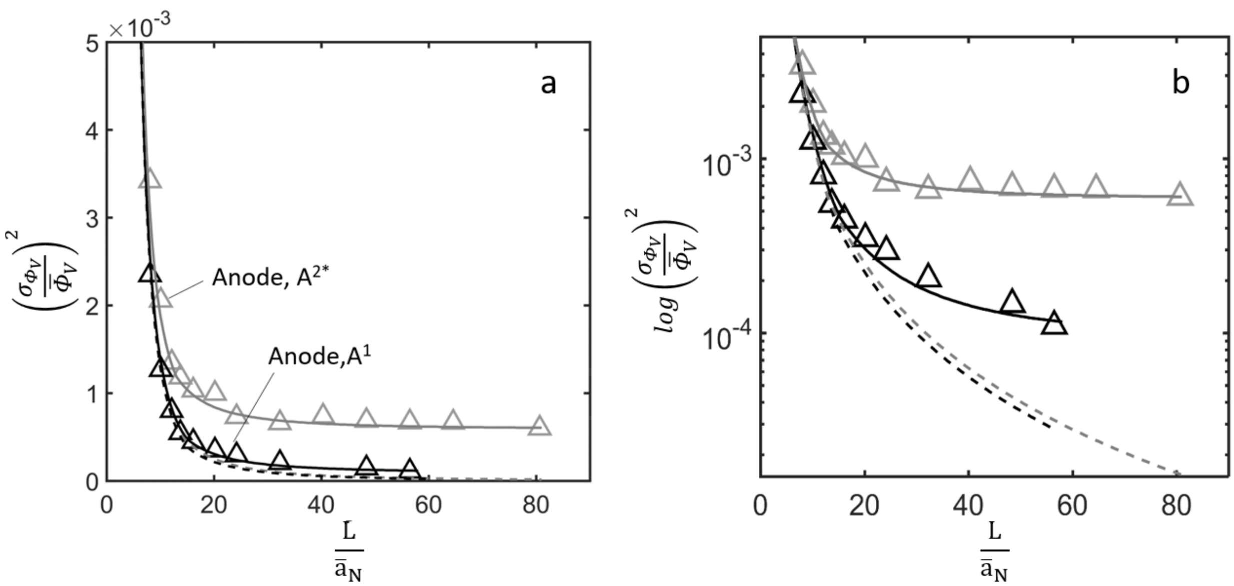

Figure 5. Rendered images of two S-$\frac{\sigma_{a_N}}{\bar{a}_N}$-$(\frac{\sigma_{\Phi_V}}{\bar{\Phi}_V})^2_{BB}$-$L_{BB}$ synthetic microstructures exhibiting simulated agglomeration of materials: a) S-0.40-4.5x10^{-2}-12.5 and b) S-0.40-3.0x10^{-1}-12.5 . The ICP is yellow, the GPP is transparent, and the ECP is blue.

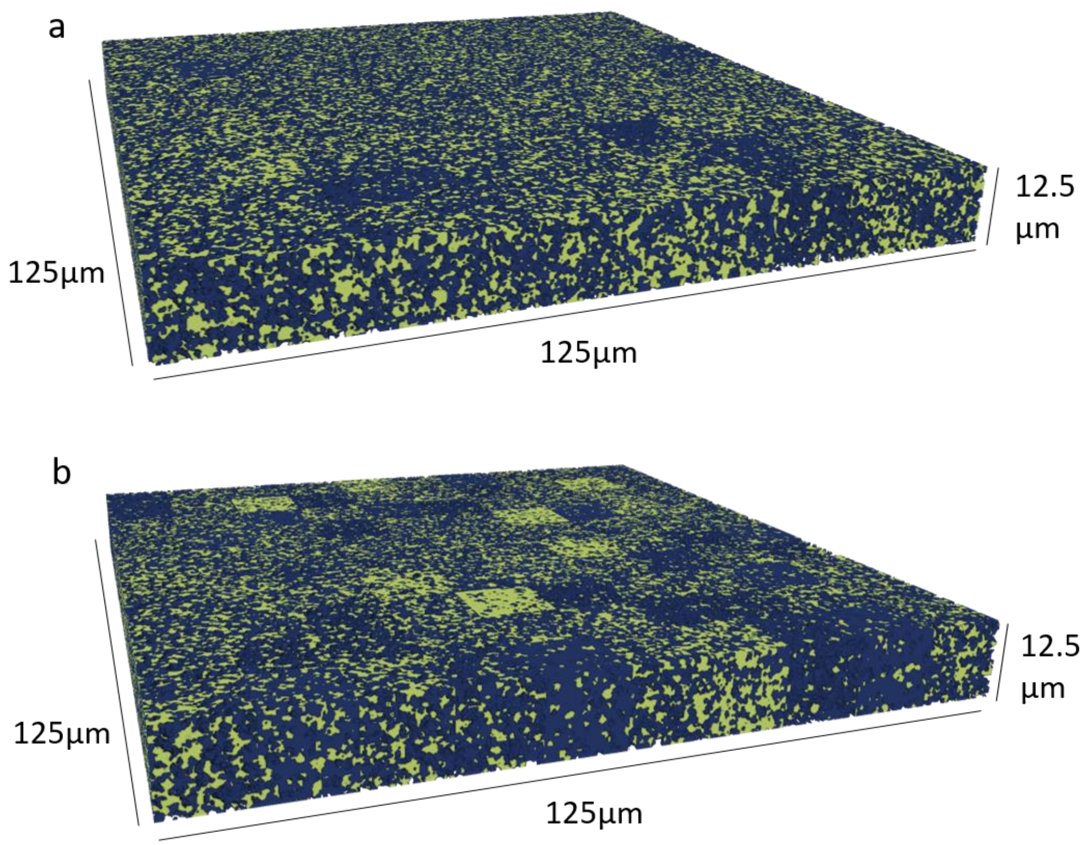

Figure 6. Mean-squared normalized variance of the aggregated phase fraction, $\left(\frac{\sigma_{\Phi_V}}{\bar{\Phi}_V}\right)^2$, plotted in linear (a, c, e) and semi-log (b, d, f) scales, as a function of the mean particle size normalized edge lengths, $\frac{L}{\bar{a}_N}$. Data points are shown for synthetic S-0.40-$\left(\frac{\sigma_{\Phi_V}}{\bar{\Phi}_V}\right)^2_{BB}$-12.5 microstructures. Fits to the data with Eq. 3 (c and d) and Eq. 4 (e and f) are shown in by similar color curved lines (fit values for A_{PSD}, A_{VFD}, B_{VFD}, and C_{L_m} are given in Table II).

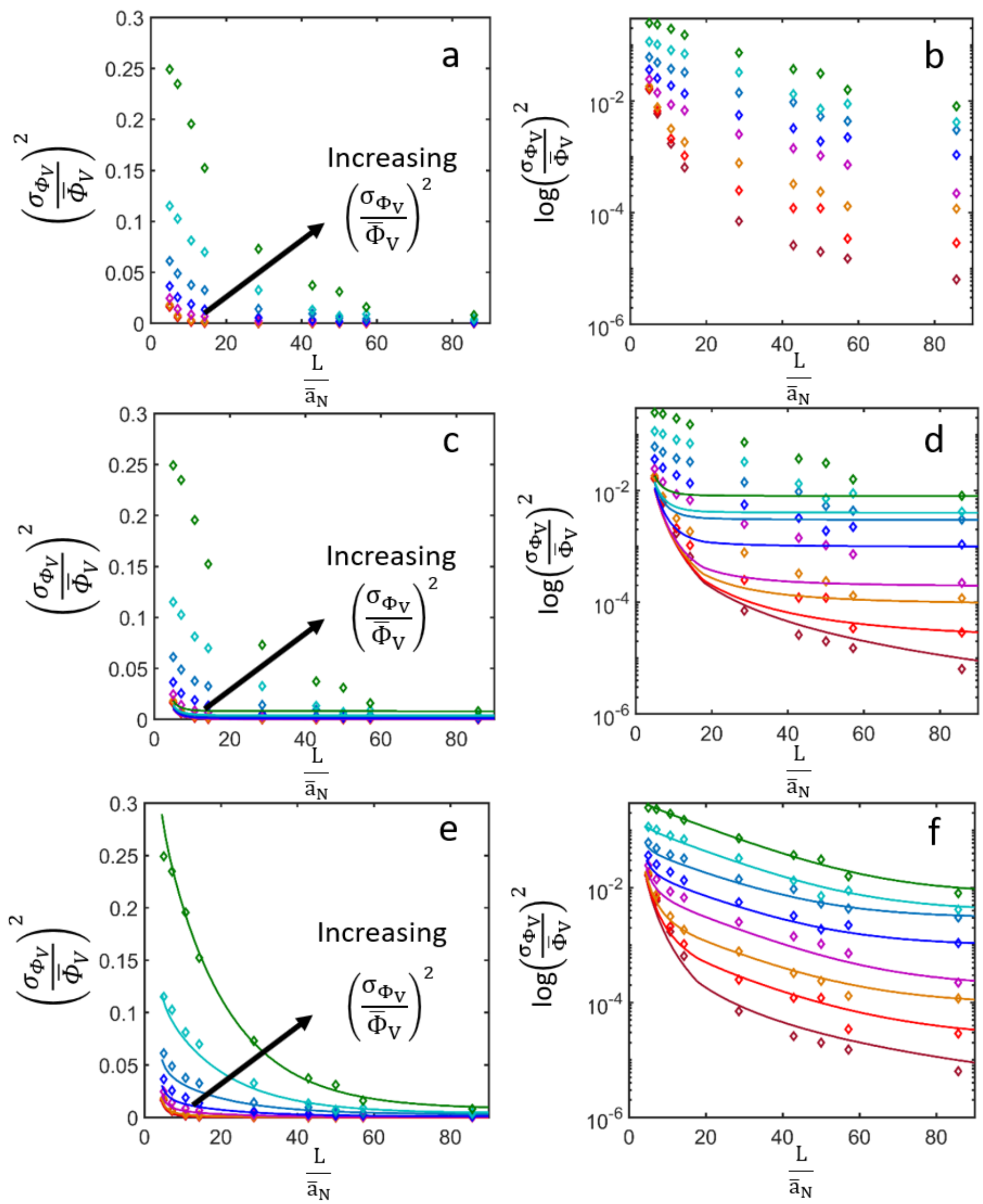

Figure 7. Mean-squared normalized variance of the aggregated phase fraction, $\left(\frac{\sigma_{\Phi_V}}{\bar{\Phi}_V}\right)^2$, plotted in linear (a) and semi-log (b) scales, as a function of the mean particle size normalized edge lengths, $\frac{L}{\bar{a}_N}$. Data points are shown for the experimental cathodes: C^1 (black), C^2 (blue), and C^{3*} (gray). Fits to the data with Eq. 4 are shown in by similar color curved lines (fit values for A_{PSD}, A_{VFD}, B_{VFD}, and C_{L_m} are given in Table III).

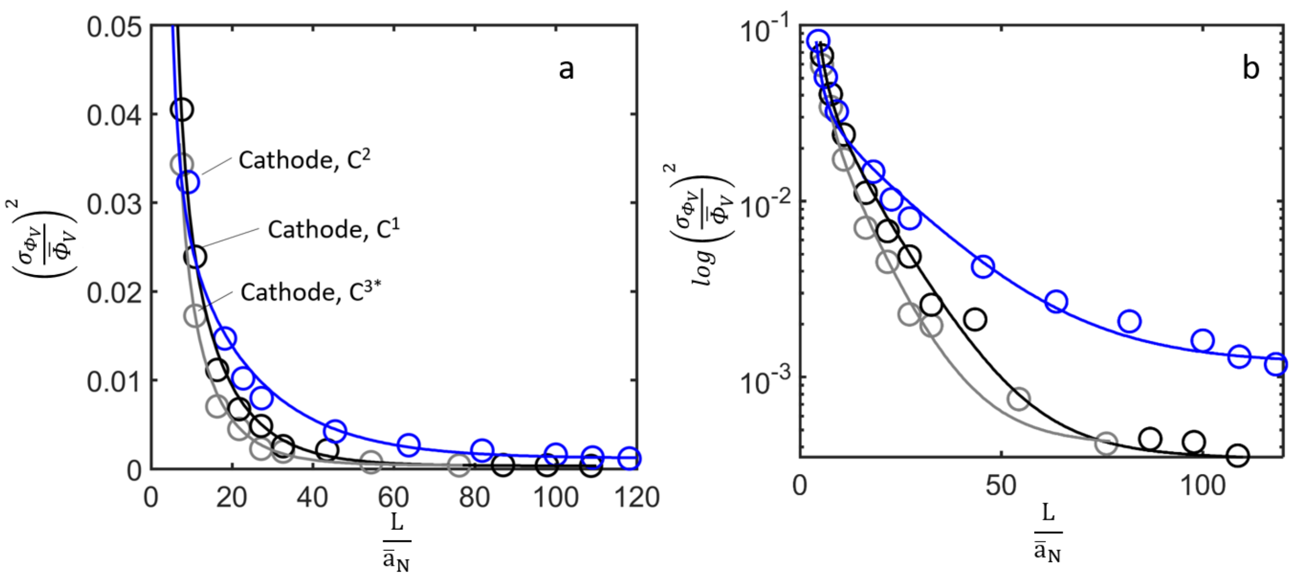

Figure 8. Comparison of mesoscale distributions of ECP volume fraction in a) Anodes, A^1 (black line) and A^{2*} (gray line) and b) cathodes, C^1 (black line), and C^{3*} (gray line) measured in t^3 sub-volumes.

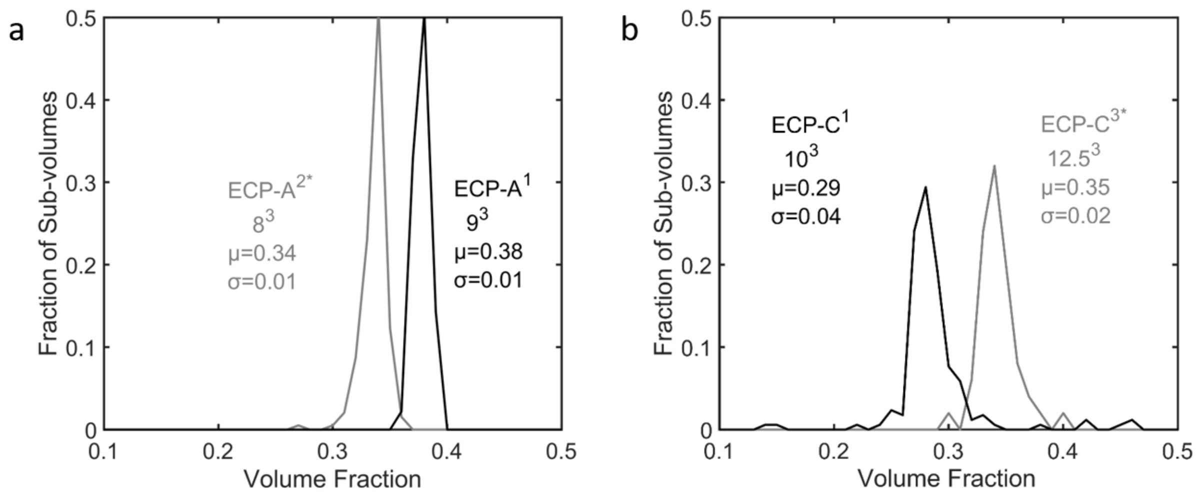

Figure 9. Comparison of mesoscale distributions of volume-weighted average electrochemical parameters measured in t^3 sub-volumes between cathodes, C^1, C^2, and C^{3*} and between anodes A^1 and A^{2*}: (a) ECP tortuosity factor, (b) TPB density, polarization resistance in the cathodes (c) and anodes (d). In figures (a) and (b) the first block compares similar distributions from the cathodes and the second block compares the distributions from the anodes.

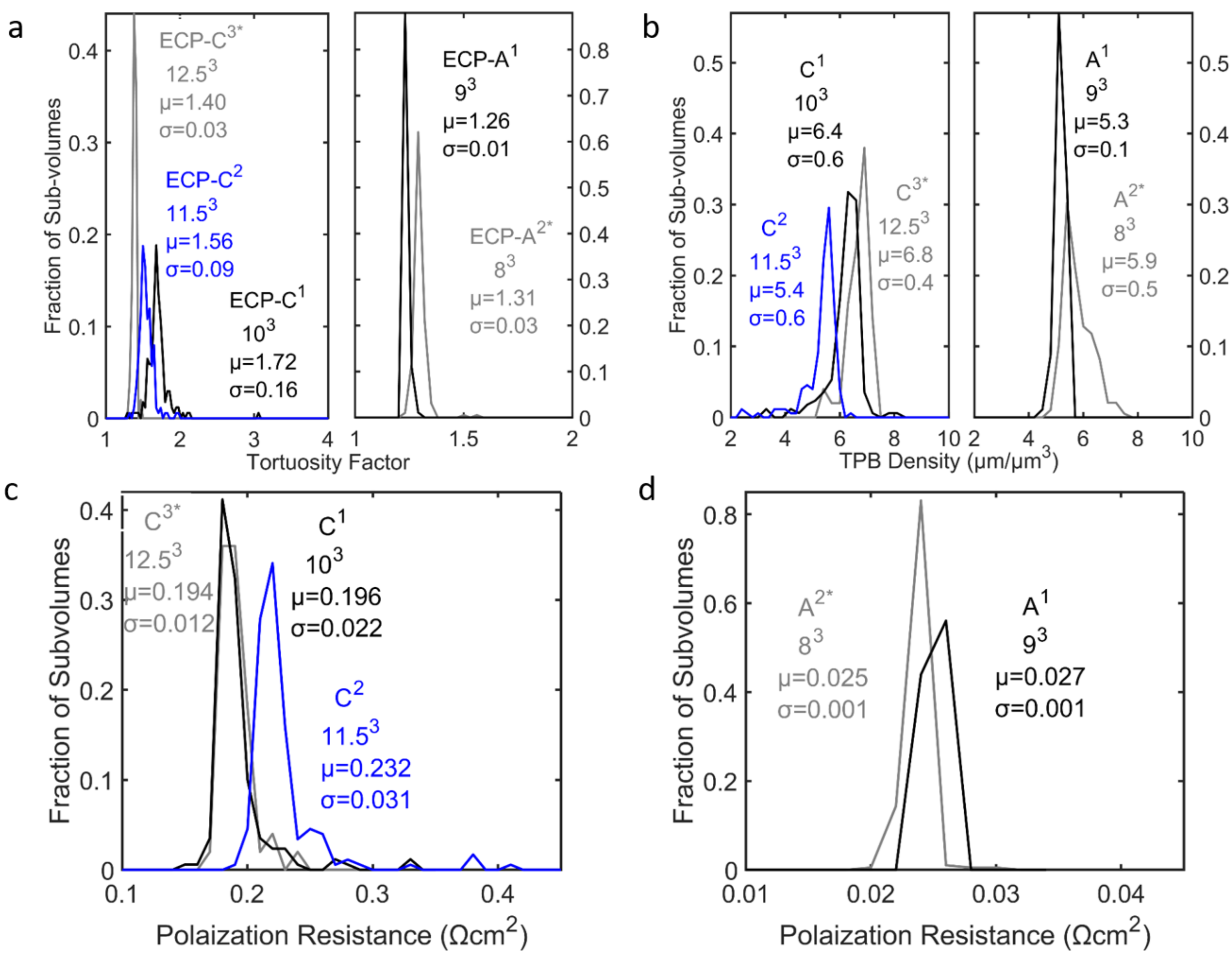

Figure 10. Predicted potential drop across the synthetic cathodes (S-$\frac{\sigma_{a_N}}{\bar{a}_N}$-$(\frac{\sigma_{\Phi_V}}{\bar{\Phi}_V})^2_{BB}$-6.25) **a)** as a function of current density for various LSM active layer microstructural heterogeneities ($(\frac{\sigma_{\Phi_V}}{\bar{\Phi}_V})^2_{BB}$) **b)** as a function of varying heterogeneity ($(\frac{\sigma_{\Phi_V}}{\bar{\Phi}_V})^2_{BB}$) of cathode active layer microstructure based on multiphysics model calculations.

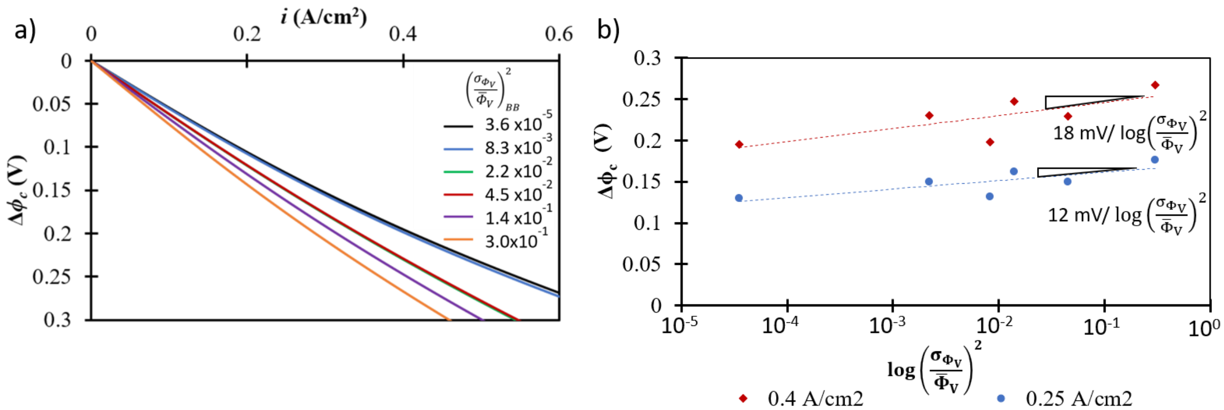

Tables

Table I. Selected statistical quantities for all four sets of synthetic microstructures.

Particle Size Distributions S-$\frac{\sigma_{a_N}}{\bar{a}_N}$				**Volume Fraction Distributions** S-$\frac{\sigma_{a_N}}{\bar{a}_N}$-$(\frac{\sigma_{\Phi_V}}{\bar{\Phi}_V})^2_{BB}$-12.5		
ln $\boldsymbol{\sigma_g^{in}}$	**$\bar{\boldsymbol{a}}_{\boldsymbol{N}}$ [µm]**	**$\boldsymbol{\sigma_{a_N}}$ [µm]**	**$\boldsymbol{\frac{\sigma_{a_N}}{\bar{a}_N}}$**	**$\boldsymbol{\sigma_{\Phi_V}^{in}}$**	**$\boldsymbol{\sigma_{\Phi_V}^{out}}$**	$(\frac{\sigma_{\Phi_V}}{\bar{\Phi}_V})^2_{BB}$
0.15 0.35 0.60 0.80	0.62 0.70 0.95 1.30	0.21 0.28 0.48 0.82	0.34 0.40 0.50 0.63	0.000	2.0 x10^{-3}	3.6 x10^{-5}
				0.075	8.0 x10^{-3}	5.9 x10^{-4}
				0.100	2.0 x10^{-2}	3.7 x10^{-3}
				0.125	3.0 x10^{-2}	8.3 x10^{-3}
				0.150	5.0 x10^{-2}	2.2 x10^{-2}
				0.175	7.0 x10^{-2}	4.5 x10^{-2}
				0.200	1.2x10^{-1}	1.4 x10^{-1}
				0.225	1.8x10^{-1}	3.0x10^{-1}

Note: $\boldsymbol{\bar{a}_N}$ and $\boldsymbol{\sigma_{a_N}}$ are the computed average and standard deviation of the number weighted particle size. $\boldsymbol{\sigma_g^{in}}$ was the input (targeted) value of $\boldsymbol{\sigma_{a_N}}$ for a given simulation. $\boldsymbol{\sigma_{\Phi_V}}$ {$\boldsymbol{\bar{\Phi}_V}$} is the standard deviation {average} of aggregated volume fraction of phases among specified building blocks having edge length of 12.5 µm. $\boldsymbol{\sigma_{\Phi_V}^{in}}$ was the input (targeted) value of $\boldsymbol{\sigma_{\Phi_V}}$**,** while $\boldsymbol{\sigma_{\Phi_V}^{out}}$ is the output (measured) value. $(\frac{\sigma_{\Phi_V}}{\bar{\Phi}_V})^2_{BB}$ represents the measured value of mean^2 normalized variance among the building blocks.

Table II. Model parameters synthetic datasets

<table>
<tr><th colspan="2">Model parameters to Eq. 2 for S-$\frac{\sigma_{a_N}}{\bar{a}_N}$ datasets</th><th colspan="5">Model parameters to Eq. 4 for S-0.40-$(\frac{\sigma_{\Phi_V}}{\bar{\Phi}_V})^2_{BB}$-12.5 datasets</th></tr>
<tr><th>$\frac{\sigma_{a_N}}{\bar{a}_N}$</th><th>$A_{PSD}$</th><th>$(\frac{\sigma_{\Phi_V}}{\bar{\Phi}_V})^2_{BB}$</th><th>$A_{PSD}$</th><th>$B_{VFD}$</th><th>$A_{VFD}$</th><th>$C_{L_m}$</th></tr>
<tr><td rowspan="2">0.34</td><td rowspan="2">7.9×10^{-1}</td><td>3.6×10^{-5}</td><td rowspan="8">1.3×10^{0}</td><td rowspan="8">5.6×10^{-2}</td><td>-</td><td></td></tr>
<tr><td>5.9×10^{-4}</td><td>1.0×10^{-3}</td><td>2.1×10^{-5}</td></tr>
<tr><td rowspan="2">0.40</td><td rowspan="2">1.3×10^{0}</td><td>3.7×10^{-3}</td><td>3.0×10^{-3}</td><td>9.0×10^{-5}</td></tr>
<tr><td>8.3×10^{-3}</td><td>9.0×10^{-3}</td><td>1.9×10^{-4}</td></tr>
<tr><td rowspan="2">0.50</td><td rowspan="2">6.1×10^{0}</td><td>2.2×10^{-2}</td><td>2.2×10^{-2}</td><td>9.9×10^{-4}</td></tr>
<tr><td>4.5×10^{-2}</td><td>5.0×10^{-2}</td><td>3.0×10^{-3}</td></tr>
<tr><td rowspan="2">0.63</td><td rowspan="2">17.7×10^{0}</td><td>1.4×10^{-1}</td><td>1.4×10^{-1}</td><td>4.0×10^{-3}</td></tr>
<tr><td>3.0×10^{-1}</td><td>3.5×10^{-1}</td><td>8.0×10^{-3}</td></tr>
</table>

Table III. Model parameters for experimental datasets

Experimental Datasets	$\bar{a}_N$	$\frac{\sigma_{a_N}}{\bar{a}_N}$	A_{PSD}	A_{VFD}	B_{VFD}	$\frac{1}{B_{VFD}}$	C_{L_m}
Anode-A[1]	0.62	0.40	$1.3\text{x}10^{0}$	0.00	-	-	$9.0\ \text{x}10^{-5}$
Anode-A[2*]	0.60	0.42	$1.3\text{x}10^{0}$	0.00	-	-	$5.9\ \text{x}10^{-4}$
Cathode-C[1]	0.46	0.50	$6.1\text{x}10^{0}$	$5.0\ \text{x}10^{-2}$	$9.0\ \text{x}10^{-2}$	11	$3.3\ \text{x}10^{-4}$
Cathode-C[2]	0.46	0.40	$1.3\text{x}10^{0}$	$4.0\ \text{x}10^{-2}$	$5.5\ \text{x}10^{-2}$	18	$1.2\ \text{x}10^{-3}$
Cathode-C[3*]	0.55	0.50	$6.1\text{x}10^{0}$	$4.0\ \text{x}10^{-2}$	$1.1\ \text{x}10^{-1}$	9	$3.9\ \text{x}10^{-4}$